

# Addressing the efficiency loss and degradation of triple cation perovskite solar cells via integrated light managing encapsulation



Seyede Maryam Mousavi <sup>a</sup>, Hamidreza Daghigh Shirazi <sup>a</sup>, Rikhard Ranta <sup>b</sup>,  
Muhammad Imran Asghar <sup>c</sup>, Severi Kasurinen <sup>b</sup>, Janne Halme <sup>b</sup>, Jaana Vapaavuori <sup>a,\*</sup>

<sup>a</sup> Department of Chemistry and Materials Science, Aalto University School of Chemical Engineering, Espoo, Finland

<sup>b</sup> Department of Applied Physics, Aalto University School of Science, Espoo, Finland

<sup>c</sup> Renewable Energy Technologies Group, Faculty of Engineering and Natural Sciences, Tampere University, Tampere, Finland

## ARTICLE INFO

### Article history:

Received 22 July 2024

Received in revised form

26 September 2024

Accepted 5 October 2024

Available online 10 October 2024

### Keywords:

Perovskite solar cell

Encapsulation

Stability

Soft lithography

Light management layer

## ABSTRACT

Here, we present a holistic encapsulation method for perovskite solar cells to address both optical performance losses at the air-cell interface as well as intrinsic and extrinsic stability challenges. Our one-step method provides shielding to PSCs from oxygen and moisture-induced degradation as well as *in situ* patterning for light management. As a result of embedding the antireflective coating onto the front side of the cell, the power conversion efficiency (PCE) of the PSCs was increased from  $14.1 \pm 0.8\%$  to  $15.6 \pm 0.8\%$ , indicating an 8% relative improvement. Moreover, the encapsulated devices kept their initial performance after 90% relative humidity and water immersion tests. The outdoor exposure test showed no degradation for the encapsulated cells after 24 h of resting at  $-17^\circ\text{C}$  and maximum wind speeds of 7 m/s on average. Additionally, the encapsulation strategy was instrumental in mitigating oxygen and humidity-induced degradation during ISOS-LC tests, retaining up to 80% of the initial performance for the encapsulated devices after 360 h. This research establishes *in situ* encapsulation and patterning as a promising solution for reducing optical losses and extrinsic instabilities in PSCs. The choice of flexible encapsulant enables it to be used for both rigid and flexible PSCs in a wide range of applications.

© 2024 The Author(s). Published by Elsevier Ltd. This is an open access article under the CC BY license (<http://creativecommons.org/licenses/by/4.0/>).

## 1. Introduction

Solar power promises to cover half of the worldwide electricity production by 2060 [1]. As a third-generation photovoltaic technology, perovskite solar cells (PSCs) are pivotal in this transformation, owing to their low manufacturing costs and high efficiency of over 26% [2]. The commercialization of the current generation of PSCs is hindered due to various degradation issues. To overcome these limitations, the next-generation PSCs must address the challenges related to their intrinsic/extrinsic stability and optical properties. The intrinsic instability, mainly, comes from the dissociation of molecular cations and ion migration of metal halide perovskites (PSKs) that can be mitigated through compositional engineering of PSK [3,4], electron [5,6] as well as hole transport layers [7,8], and/or electrodes [9,10]. The low activation energy for ionic migration within PSCs allows organic components to migrate from the inorganic octahedral network, leading to the formation of

vacancy defects. These defects amplify the overall sensitivity of PSKs to environmental factors, such as moisture, oxygen, illumination, and heat [11,12]. Moisture breaks PSK's hydrogen bonds and consequently forms hydrated compounds through the creation of new hydrogen bonds [13]. Through this mechanism, moisture catalyzes the irreversible decomposition of the PSK absorber, which can be further intensified by illumination [14,15]. Furthermore, the creation of charge barriers and electronic traps occurs by oxygen reacting with PSK ions. Further oxygen degradation can be induced through the formation of superoxide species at the surface of the PSK leading to performance loss of the devices [15,16].

From the efficiency perspective, the device performance suffers from optical loss due to reflection at the interface between the PSC and its surrounding environment, which reduces the incident light to the absorber layer [17]. To minimize these losses, surface texturing strategies have been employed. Such strategies could also introduce haze, resulting in light scattering in multiple directions, extending the optical path and thus, effectively enhancing light absorption within the active layer of PSCs [18–23].

Numerous studies have demonstrated the application of polydimethylsiloxane (PDMS) for protecting optoelectronic devices

\* Corresponding author.

E-mail address: [Jaana.vapaavuori@aalto.fi](mailto:Jaana.vapaavuori@aalto.fi) (J. Vapaavuori).

from environmental factors, particularly moisture, due to its excellent moisture and oxygen barrier properties. However, these studies often utilized either high temperatures, resin-based glues, or intricate techniques such as atomic layer deposition to achieve this protection [12,24–27]. Furthermore, PDMS's suitable refractive index and moldability make it highly effective for use in PSC patterning [28]. Therefore, PDMS is an excellent candidate for encapsulating and patterning PSCs.

Considering optical losses and the instability issues of PSCs, an ideal encapsulation should address both problems concurrently without requiring high temperatures, UV curing [25], and/or intricate techniques [24] as these can severely impact the performance of PSCs [12]. Therefore, the present work employs PDMS as an encapsulant to provide a holistic and straightforward technique that in one step enhances the performance and stability of PSCs. The *in situ* encapsulation combined with the patterning approach employs soft lithography to introduce a simple path that enhances the stability and performance of PSCs. Furthermore, this process operates at room temperature without requiring heating or UV curing.

In the presented method, the entire surface and sides of the solar cells were coated with PDMS, and the front-facing surface of the PSC was *in situ*-patterned using a soft lithography technique. A replica of leek leaf surface structures was created on the PDMS to reduce reflection and increase haze. Leek leaf replicas, previously used as add-on layers for PSC devices, have shown promise due to their optical and self-cleaning properties [29]. To evaluate the effects of encapsulation and patterning, the devices were first encapsulated, and their performance and stability were assessed. Then, the performance was reassessed after adding the leek leaf surface structure to the front side. This unified approach of combining encapsulation and surface patterning not only provided a barrier against oxygen and moisture but also simultaneously improved solar cell efficiency by reducing reflection and increasing haze.

## 2. Methodology

### 2.1. Materials

Polydimethylsiloxane (PDMS, Sylgard™ 184 silicone elastomer kit, Dow Chemical Co., USA), aluminum foil (local market), Silvar paint ethanol (Etax A7, Altia Industrial Oyj, Finland), toluene (99.8 %, Sigma-Aldrich, Germany), fluorine-doped tin oxide glass substrates (Greatcell solar, TEC15), TiO<sub>2</sub> paste (30 NR-D, Dyesol), acetylacetone (Sigma-Aldrich, P7754), titanium diisopropoxide (Sigma-Aldrich), lead iodide-PbI<sub>2</sub> (TCI, L0279), lead bromide-PbBr<sub>2</sub> (TCI, L0288), cesium iodide-CsI (abc GmbH, AB207757), formamidinium iodide (Greatcell ethylammoniumylamonium bromide (Greatcell solar), dimethylformamide-DMF (anhydrous-Sigma-Aldrich), dimethyl sulfoxide-DMSO (anhydrous-Sigma-Aldrich), chlorobenzene (anhydrous-Sigma-Aldrich), acetonitrile (anhydrous-Sigma-Aldrich), Spiro-OMETAD (Sigma-Aldrich), tert-butylpyridine-tBP (Sigma-Aldrich), Lithium bis(trifluoromethanesulfonyl)imide-LITFSI (Sigma-Aldrich), FK 209 Co(II) PF<sub>6</sub> salt (Sigma-Aldrich), gold (Kurt J. Lesker Company), leek (local market), 1H,1H,2H,2H-Perfluorododecyltrichlorosilane (Sigma-Aldrich), silver conductive paste (Electrolube) were used without further purification.

### 2.2. Device fabrication

FAMACs-based PSCs were fabricated using the spin coating fabrication technique.<sup>[95]</sup> The fabrication procedure follows the recipe published by Saliba et al. with minor changes [30]. First, the pre-cut (1.4\*2.4 cm<sup>2</sup>) fluorine-doped tin oxide glass substrates were etched using a laser scribe (Epilog Laser Zing 35 W). Then

substrates were washed with detergent, rinsed with deionized water, and 15 min sonication in all the following solvents, Hellmanex diluted in deionized water (2 %), ethanol, and isopropanol, successively. After drying in a hydrothermal oven (Hydrothermal Oven Memmert 100–800) at 120 °C to avoid stains, the substrates were treated with UV ozone cleaning to ensure the removal of organic residuals and improve the surface wettability. TiO<sub>2</sub> compact layer (c-TiO<sub>2</sub>) was deposited on 20 pieces of pre-cut fluorine-doped tin oxide (FTO) substrates by spray pyrolysis of the solution containing acetylacetone (0.4 mL), titanium diisopropoxide bis(acetylacetonate) (0.26 mL) in 6 mL of ethanol at 450 °C. A mesoporous TiO<sub>2</sub> (m-TiO<sub>2</sub>) scaffold layer was deposited on top of the c-TiO<sub>2</sub> by spin coating the dispersion of 30NRD TiO<sub>2</sub> paste in ethanol (150 mg TiO<sub>2</sub> paste in 1 mL ethanol) at 4000 rpm for 10 s, then annealing at 450 °C. After cooling down to room temperature, the samples were transferred to the nitrogen-filled glovebox. In order to make the triple cation perovskite first the 1.5 M PbI<sub>2</sub> and PbBr<sub>2</sub> stock solutions were prepared in anhydrous DMF: DMSO (4:1, v:v) and heated up to 180 °C. The FAPbI<sub>3</sub> solution was prepared by adding PbI<sub>2</sub> (1.1 M) to formamidinium lead iodide (1.08 M) powder. The MAPbBr<sub>3</sub> solution was prepared from a precursor solution containing MABr (0.22 M) and PbBr<sub>2</sub> (0.24 M) powder. CsI powder was dissolved as a 1.5 M stock solution in DMSO. The precursors were then mixed in (FAPbI<sub>3</sub>/MAPbBr<sub>3</sub>/CsI) 83:17:5 volume ratios. The final precursor solution was spin coated on the mesoporous layer in the following two steps: i) 10 s at 1000 rpm and 200 rpm/s and ii) 20 s at 6000 rpm and 2000 rpm/s. Ten seconds before the second-step completes, 150 µL of chlorobenzene was poured on the spinning substrates. Then, the substrates were annealed for 45 min at 100 °C. To form the hole transport layer (HTL), 50 µL of the HTL solution reported elsewhere [30] was dropped onto prepared PSC films and spin coated at 4000 rpm for 10 s. Then 80 nm of gold was thermally evaporated (Moorfield minilab 090) on the HTL layers. To ensure a better electrical connection, the electrodes were painted with silver paste.

### 2.3. Encapsulation and coating

Before the encapsulation, the electrodes of the PSCs were extended by using commercial conductive aluminum tape so that their performance could be monitored after they were fully covered. The aluminum tape strips were adhered to the Au electrodes and the non-conductive gap caused by the adhesive part of the tape was bridged by painting it with a conductive silver paint. The encapsulation was performed by dipping the PSCs in a mixture of PDMS with a monomer to curing agent ratio of 5:1 volume ratio. The PSCs were then sandwiched between a glass coverslip from the gold electrode side and a negative antireflective mold from the bottom (glass side) of the substrates, and the edges of the substrate were covered with 0.5 mL of PDMS. The PDMS was then cured at room temperature for 48 h and the negative mold was removed after curing for 48 h at room temperature. The negative mold was fabricated by replicating the surface structures of leek leaves in a similar manner presented by Daghigh Shirazi et al. [29]. For this means, first leek leaves were cut into 3 cm × 3 cm pieces and attached to the bottom of a petri dish. The leaf surfaces were subsequently covered with PDMS and allowed to be cured at room temperature for 48 h. The negative mold was then plasma-cleaned for 60 s at 100 % power by a Henniker Plasma HPT-100. The plasma-treated negative molds were then placed in a closed Pyrex petri dish followed by vapor deposition of 1H,1H,2H,2H-perfluorododecyltrichlorosilane as an anti-adhesion coating on a hot plate at 85 °C for 120 min.

#### 2.4. External quantum efficiency measurement

The external quantum efficiency (EQE) of the PSC devices was recorded using a Solar cell spectral response measurement system (QEX7 Serial #81) (PV measurements, INC).

#### 2.5. Operational stability measurement

To evaluate the operational stability of the devices, the ISOS-LC1 protocol was employed. For that, five various devices underwent 8 h of 1 sun illumination daily, followed by an overnight resting period. The current density (J)–voltage (V) performance of the cells was measured both before and after the illumination cycle to assess recovery rates and degradation times. The current (I)–voltage (V) characteristics of the cells were measured using a Keithley 2450 source measure unit, under air mass 1.5G simulated sunlight (100 mW/cm<sup>2</sup>). The sun simulator was calibrated with a silicone reference solar cell and a shadow mask with 0.16 cm<sup>2</sup> area was employed for the measurement. The reported graphs are the average of reverse and forward bias J–V scans.

#### 2.6. Long-term stability measurement

The evaluation of the long-term stability (shelf-life) was conducted by continuously monitoring the efficiency of five various devices over 2300 h, which was adopted from the ISOS-D protocol. The following three scenarios were investigated: control device in a dark glovebox atmosphere, pristine device, and encapsulated devices which were continuously exposed to ambient conditions (25 ± 4 °C and relative humidity (RH) 42 %).

#### 2.7. Photo booth for color-calibrated images

The imaging system comprises off-the-shelf components, employing a mirrorless camera with optimized color accuracy settings. Images were captured in RAW format with low ISO, high aperture, and a macro lens for a resolution of about 4.5 μm per pixel. LED panels provided uniform illumination, and corrections were applied for distortions and uneven lighting. Exported in high-bit-depth TIFF (Tag Image File Format), images underwent color correction in open source software calibrated with IT8.7 targets. Post-correction, color deviations average less than 1.0 CIEDE2000 from known calibration values. This ensures sustained color accuracy, enabling precise measurements and correlations with other data. The system yields realistic images compared with higher resolution but less color accurate microscope images.

#### 2.8. Characterization of the antireflective coating

The optical properties of the antireflective coatings were characterized using UV-2600 UV–vis spectrophotometer with ISR-2600Plus integrating sphere attachment (Shimadzu, Japan). The total light transmittance, haze, and reflectance were measured for 300 nm–900 nm wavelengths, and the average and standard deviations were reported for three sets of measurements. The transmittance and haze were calculated using the following equations:

$$\text{Transmittance (\%)} = T_2/T_1 \times 100 \quad (1)$$

$$\text{Haze (\%)} = (T_4/T_2 - T_3/T_1) \times 100 \quad (2)$$

where  $T_1$  is the reference transmittance measured with no sample,  $T_2$  is the measured transmitted light intensity through the sample,  $T_3$  is beam scattering with no sample,  $T_4$  is the diffusive transmittance measured through the sample.

The reflectance was calculated using the following equation:

$$\text{Reflectance (\%)} = R_2/R_1 \times 100 \quad (3)$$

where  $R_1$  refers to the reflectance measured with the reference (white background), and  $R_2$  is the measured reflectance in the presence of the sample.

The surface structures were imaged using a scanning electron microscope (SEM, Tescan Mira3). Before the measurement, the samples were first sputter coated with 5 nm of Au/Pd (80/20) using Q150T coater (Quorum).

### 3. Results and discussion

Fig. 1 schematically illustrates the fabrication process of anti-reflective PDMS-encapsulated devices (AR-PED). The PSC device substrate was dipped in the sealant in order to protect the edges and sides from water and oxygen penetration and it was sandwiched between the fabricated negative mold and the glass coverslip to allow *in situ* encapsulation and patterning of the glass side for prevention of optical losses.

The encapsulation process was coupled with soft lithography to create a light management layer for the PSC architecture presented in Fig. 2a. Fig. 2b presents a photograph of the complete AR-PED assembly. Although patterning and encapsulation are conducted simultaneously and as one-step, this study is structured to investigate the impact of each independently. This division allows for a systematic examination of the effectiveness of encapsulation on stability and the influence of light management coating on overall performance. We first present the results from the durability tests for the PDMS-encapsulated devices (PED) and thereafter discuss how adding the antireflective coating on PDMS-encapsulated devices (AR-PED) affects the photovoltaic performance. As summarized in Table S1, although the encapsulation improved the current density of the devices, it had statistically no significant change (<1 %) in the efficiency of the devices. The appearance of the PED looked seamless after the encapsulation (Fig. S1a and b), whereas applying other sealants such as epoxy visibly degraded the devices possibly due to the exothermic curing reactions (Fig. S1c) [12].

The moisture barrier efficacy and protective capabilities of encapsulation were assessed by exposing the devices to elevated humidity levels of 90 % at room temperature in the dark. Fig. 3a reveals that pristine devices underwent near-complete degradation and complete transformation to PbI<sub>2</sub> within 3 h of the damp test, whereas the PED retained their initial photovoltaic characteristics even after 6 h of exposure to elevated humidity levels. The photographs in Fig. S2 taken from samples at each stage of aging correlate well with the performance data in Fig. 3a. The PED shows no color change, while the degradation in the pristine device is evident in both the photographs and the performance data.

As is evident in Fig. S2, during the first hours of the test, the humidity caused the formation of yellow spots in the pristine PSC devices. The initial formation of small yellow spots on the surface of PSCs can be indicative of localized degradation processes which can act as nucleation sites for facilitating the decomposition by reaching the grain boundaries and forming hydrates within the PSK film [31]. In an additional evaluation of moisture barrier properties, the very same PEDs were immersed in water for over 1 h. In contrast to the pristine samples, which were completely decomposed, the encapsulated devices maintained their performance, reaffirming the effectiveness of the encapsulation in protecting against moisture and water immersion.

To explore the oxygen barrier properties of the encapsulation, the devices were kept in the outdoor environment to mimic the ISOS O1 [32] protocols. Conducted during winter (January) in

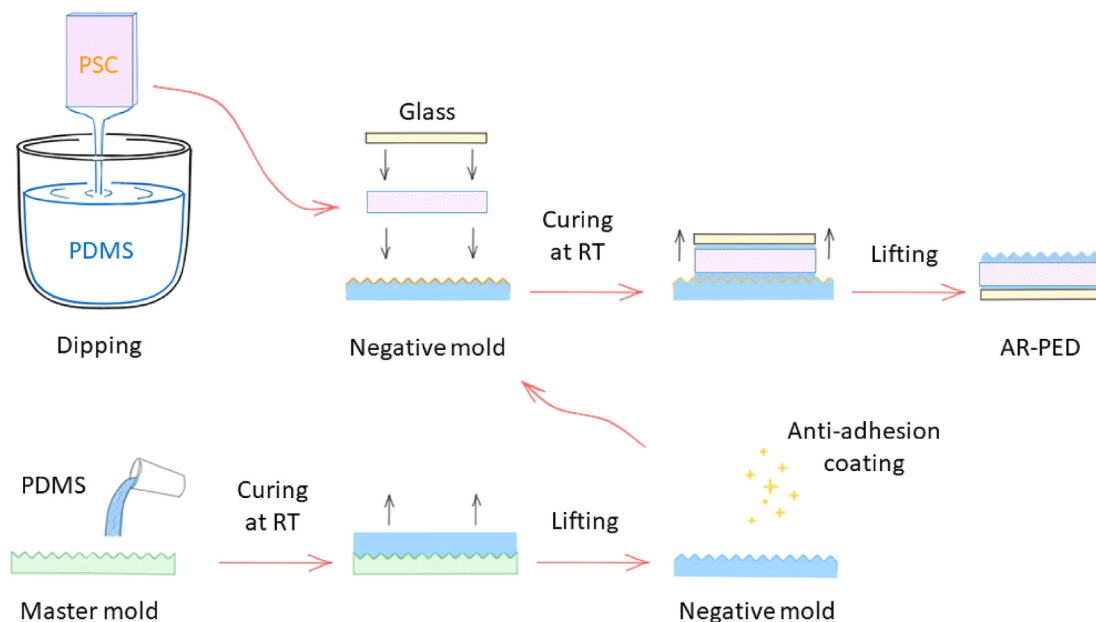


Fig. 1. The fabrication process of AR-PED. AR-PED: antireflective polydimethylsiloxane-encapsulated devices.

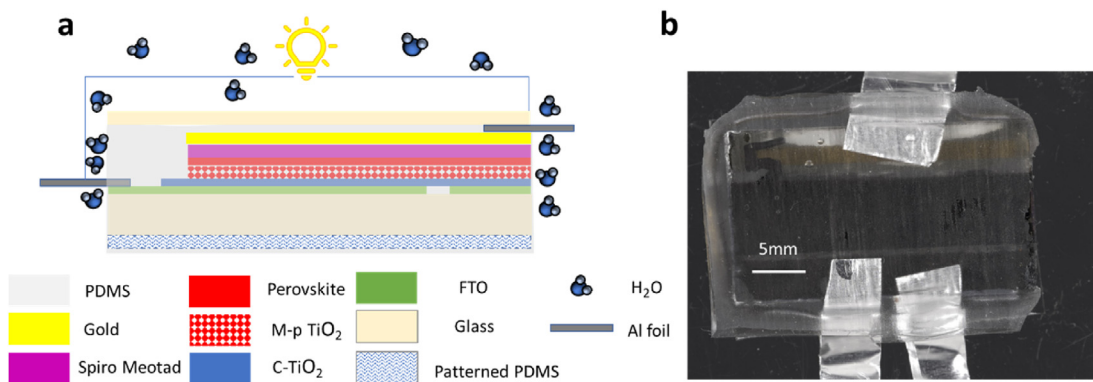


Fig. 2. a) The schematic architecture and b) the image of the AR-PED. AR-PED: antireflective polydimethylsiloxane-encapsulated devices.

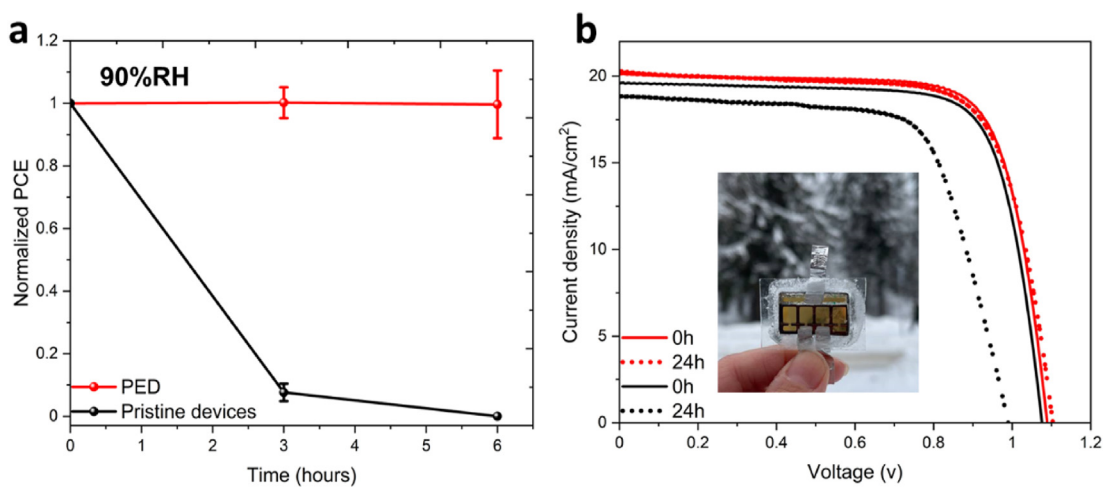


Fig. 3. a) Normalized PCE vs time graphs of the 90% RH test, b) The J-V behavior of PED (red) and pristine champion devices (black) before and after 24 h of rest outdoors at  $-16\text{ }^{\circ}\text{C}$  (inset is the image of PED after aging). PCE: power conversion efficiency; PED: polydimethylsiloxane-encapsulated devices.

Espoo, Finland, the outdoor conditions were characterized by cold and frozen weather, typical for Nordic settings. The experiment was carried out at an average temperature of  $-17\text{ }^{\circ}\text{C}$  with RH of 81.28 %, with an average wind speed of 7 m/s. The averages are taken from the hourly values that are reported by the Finnish Meteorological Institute. Therefore, the test combined effective factors of freezing temperatures, oxygen, and humidity present in outdoor conditions. As can be seen in Fig. 3b, the J-V behavior of the champion PED remained almost unchanged after 24 h of resting outdoors at  $-16\text{ }^{\circ}\text{C}$ . This can also be seen in Table 1 which summarizes the average photovoltaic parameters and the standard deviations for both PED and pristine devices.

According to Table 1, after 24 h, a 12 % performance loss is observed in the pristine devices mainly due to the drop in  $V_{oc}$  and fill factor (FF). In line with the literature, it is reported that lower temperatures decrease the FF, a trend which is also evident in our study. Specifically, the FF decreased in the pristine devices while the PEDs maintained their FF due to the effect of encapsulation. The observed decrease in  $V_{oc}$  and the adverse effects on device performance are proposed to be attributed to the generation of superoxide due to oxygen-accelerated photodegradation. The superoxide, produced when oxygen accepts a photoexcited electron from the perovskite, fills the defect sites e.g. iodine vacancies, and reacts with the free ions inside the lattice [33,34]. This phenomenon, occurring in the presence of oxygen and illumination, is responsible for the observed adverse effects on device performance, including the decrease in  $V_{oc}$  and the overall performance loss [35,36]. This can also be seen in Fig. S3b, which reveals the addition of new small yellow dots and clusters on the aged pristine device that are not present in the encapsulated devices. Fig. S5a represents the fresh pristine device provided for comparison purposes. As documented in the literature, lower temperatures have been observed to decrease the FF, impacting pristine devices more significantly compared with PEDs, where the FF exhibited a slight decrease [12,37,38].

To ensure operational stability and explore the impact of encapsulation on protection from oxygen and moisture-induced photodegradation, the PSC devices were subjected to aging conditions following the ISOS-LC protocol [32]. According to the ISOS-LC1 protocol, the devices underwent illumination at 1 sun intensity for 8 h per day, followed by a 16-h resting period both at about  $30\text{ }^{\circ}\text{C}$  and about 42 % RH. This controlled cycle enabled us to evaluate and observe the recovery rate of the devices, which could be affected by the oxygen and moisture in the ambient air. Illustrated in Fig. 4a, the degradation and recovery rates of photovoltaic parameters of both PEDs and pristine devices are comparable up to 70 h. However, beyond this point, the pristine devices tend to degrade more rapidly under illumination, with their degradation rate surpassing their recovery rate, resulting in a rapid decline to 40 % of their initial performance over 360 h. This irreversible degradation stems from combining the effects of oxygen and more importantly humidity with illumination [39].

**Table 1**

The average and standard error of photovoltaic parameters of four PED and pristine PSC devices before and after aging at a temperature of  $-16\text{ }^{\circ}\text{C}$  with an RH of 10 %.

	Aging	PCE	$J_{sc}$	$V_{oc}$	FF
PED	Before	$15.1 \pm 0.9$	$19.7 \pm 0.5$	$1.08 \pm 0.01$	$0.71 \pm 0.04$
	After	$15 \pm 0.9$	$19.8 \pm 0.4$	$1.08 \pm 0.02$	$0.70 \pm 0.02$
Pristine devices	Before	$15 \pm 0.8$	$19.6 \pm 0.2$	$1.05 \pm 0.02$	$0.73 \pm 0.03$
	After	$13.1 \pm 0.6$	$19.3 \pm 0.6$	$0.99 \pm 0.01$	$0.68 \pm 0.02$

PED: polydimethylsiloxane-encapsulated devices; PCE: power conversion efficiency; RH: relative humidity.

The previous research has suggested that light-induced halide segregation, illumination-derived ion migration, and compositional degradation can happen in the PSCs due to defects in the PSK lattice's bulk, surface, or grain boundaries [12,40]. While this phenomenon can be reversible to some extent, it is demonstrated that the formed defects can irreversibly spread under a humid environment [15]. Moreover, the interaction between photo-generated electrons and oxygen, which yields PbO as the final photodegradation product, is also a critical factor in the observed photodegradation of pristine devices [40]. In contrast with the pristine devices, PEDs kept nearly 80 % of their initial performance after more than 360 h of the aging test. As shown in Fig. 4a, on average, the PCE of the PEDs decreased during the illumination period and the majority of the reduction was recovered during the resting time. The same trend is also evident in Fig. 4b and c presenting  $J_{sc}$  and FF values of PEDs, whereas, as can be seen from Fig. 4d, the  $V_{oc}$  remained constant over time. This can be explained by the fact that the photodegradation of PSCs leads to a decline in PCE and the decreased performance would be recovered to a certain extent in the dark [41], which supports the idea that reversible reactions dominate the photodegradation process of the PEDs [42]. As was shown in earlier moisture and oxygen tests, the PDMS encapsulation guarantees full protection against oxygen and humidity exposure, so the PEDs' initial PCE loss could potentially stem from the intrinsic instability of the PSC devices as well as from the photo-induced ion migration and displacement [41]. In order to compare the visual changes in the appearance of the PEDs and pristine PSCs after aging, an image of a fresh PSC device is shown in Fig. 4e. Fig. 4f reveals that the original appearance of the PEDs remained unchanged after the aging process. In contrast, Fig. 4g shows a notable decolorization in the aged pristine devices, indicating a visual clue of the PSK's degradation to non-PSK phases. Interestingly, the pristine PSC devices aged under humidity and light showed severe signs of decolorization, while those in elevated humidity and water immersion turned yellow. This distinction likely arises from different degradation pathways of PSK in dark and humid environments compared with illuminated and moist conditions. As described by Nakamura et al. [39], in the presence of light and humidity, PSK generates  $\text{CH}_3\text{NH}_3\text{I}$  and  $\text{NH}_4\text{PbI}_3 \cdot 2\text{H}_2\text{O}$  which surpasses the degradation of PSK into  $\text{PbI}_2$  or in simpler terms, turning yellow. According to the results of the tests in various environmental conditions representing summer, winter, and mild weather conditions, the PDMS encapsulation at room temperature successfully removed moisture and oxygen from the degrading factors and kept the PSK integrity and the PSCs' performance over various aging conditions.

To further confirm our observations and assess the encapsulation's resistance to harsh environmental conditions, the devices underwent a photostability test following the ISOS-LC-3 protocol [32]. The results, detailed in Fig. S4, illustrate nearly complete degradation and discoloration of the pristine devices after approximately 343 h of exposure to  $780\text{ mw/cm}^2$  (UV irradiation equivalent to 1 sun) at around  $60\text{ }^{\circ}\text{C}$  and 70 % RH. In contrast, the PEDs retained approximately 65 % of their initial PCEs. The decolorization effect indicating the degradation of the PSCs [43] is evident in both the encapsulated and unencapsulated devices. Nevertheless, the bleaching impact is notably reduced in the encapsulated devices compared with the pristine devices due to the protective barrier provided by encapsulation against oxygen and moisture, effectively slowing down photodegradation [44,45]. Visual evidence from the images of the encapsulated devices (see Fig. S4 c, d) confirms this, showing less discoloration and maintaining 65 % of their initial performance, in contrast to the pristine devices which maintained only 20 % of their initial performance.

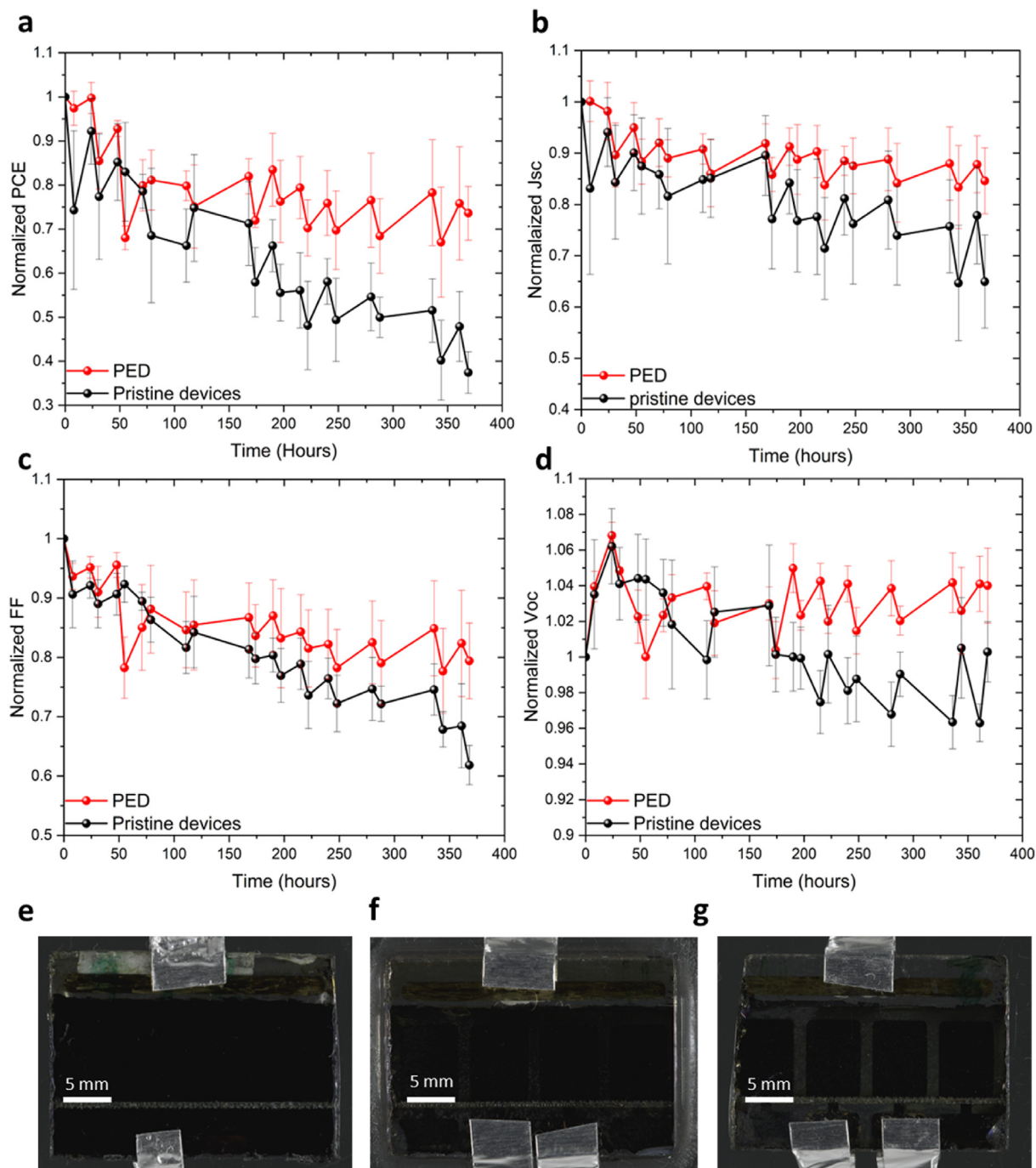


**Fig. 4.** The evolution trend of the normalized a) PCE, b)  $J_{sc}$ , c) FF, d) Voc, of PED and pristine PSC devices over 360 h of light cycle test. Images of e) fresh device, f) PED after aging, g) and pristine device after aging. PED: polydimethylsiloxane-encapsulated devices; PSC: perovskite solar cell.

Furthermore, it is noteworthy that the degradation trend at the first 24 h of the test showed no degradation in the PEDs at the test condition while the pristine devices already lost 60 % of their PCE. This observation highlighted the following two important findings: i) lower light intensities help to keep the performance of PEDs and confirm the detrimental effect of light intensity highlighting the need for improving the photostability and ii) encapsulation's strong sealing ability to protect the devices from elevated moisture ingress at high temperatures.

The dark storage ISOS-D1 test was carried out to specifically evaluate if the encapsulation can protect the devices from early

degradation due to ambient conditions, particularly in a humid summer environment. To test it, a group of PEDs and pristine devices' performance at 25 °C (max. 30 °C) and 42 % RH (max. 80 %) were compared with the ones kept in the inert atmosphere. The results showed that the PEDs behaved the same as the devices that were kept in the inert atmosphere, while, as Fig. 5a shows, the pristine devices had dramatical changes in their performance over time and their PCEs dropped below that of control, and the PEDs from the early hours of the experiment to about 95 % of their initial performance after 1800 h solely due to the ambient oxygen and humidity.

Images of the PSC devices in various aging steps were taken to record the evolution of the change in PSC appearance. The last photos of the devices are provided in Fig. 5 for comparison. The appearance of PSC devices kept in an inert atmosphere (Fig. 5b) and the PEDs stored under ambient conditions (Fig. 5c) remained unchanged, whereas the pristine devices started to show severe degradation signs that is evident in Fig. 5d. Fig. 5e is an enlargement of Fig. 5d which illustrates the introduction of new degraded spots and patterns on the pristine PSC device stored under ambient conditions. The new yellow spots in Fig. 5e highlight the formation of grain boundaries that facilitate the degradation by creating major degradation pathways.

From the PCE perspective, the suitable refractive index (RI) of PDMS enables its effective utilization in fabricating light management layers, particularly in creating gradient RI structures with both glass and air [46]. Replicating the surface structure of plant leaves has been previously reported to promote multifunctional properties such as haze and self-cleaning [29,47]. The usage of the replicated leaf surfaces was confirmed to enhance the PCE of PSCs up to 6 % by applying them as add-on cellulose acetate layers [29]. In this work, the same approach was adopted to PDMS, which offers transparency, suitable RI, chemical inertness, and robustness. To decrease the reflection losses of the PSCs, the surface pattern of a leek leaf was directly replicated on the PDMS coating. For this means, a soft lithography approach was chosen for its versatility and reproducibility, enabling convenient *in situ* encapsulation and fabrication of light management coating for PSCs. The optical properties and surface structure of the coating as well as the resulting PCE improvement of AR-PED are presented in Fig. 6.

Fig. 6a shows that the addition of the patterned coating slightly reduces the total light transmittance of the FTO glass from 84 % to 80 % at 550 nm. On the other hand, the FTO glass with the patterned PDMS coating shows a significant improvement in haze reaching 55 % at 550 nm (Fig. 6b), while the bare FTO glass showed virtually no haze. The influence of the surface pattern is also noteworthy for

the reflectance, where the coating could successfully reduce the reflectance to less than half and consequently increase the EQE of the devices over the visible wavelength region (Fig. 6c). Fig. 6d shows that the combination of the relatively high transmittance, significantly higher haze, and reduced reflectance instantly improves the PCE of the AR-PED by  $8\% \pm 0.8\%$  as compared with that of PEDs.

As the photovoltaic parameters of the PEDs and AR-PEDs indicate (see inset of Fig. 6d), the PCE improvement was attributed to about 6 % enhancement in the short current density and the consequent 2 % open circuit voltage improvement. This enhancement suggests that the lower reflection loss combined with longer light paths due to higher haze improved the light harvesting by the AR-PEDs. Fig. 6e–f present the lateral view of the patterned coating, showing the morphology of the surface structure and the thickness of the coating, revealing a thickness of ca. 400 nm. During the soft lithography process, surface features in sub-/micrometer-scales are translated to PDMS surface, governing the optical properties. These surface structures resemble the surfaces with a combination of microscale and nanoscale features, which are often tailored for efficient light scattering and antireflection [48–50]. Such structures are known to form a gradient of RI profile at the air-solid interface and effectively reduce the surface reflection [51,52]. For comparison, the SEM images including the top view of the leek leaf and replicated surface morphology are presented in Fig. S5. The SEM images confirm the replication of the surface features, including the grooves and stomata typically observed on leek leaves, and while some variations may exist among individual leaves, the results align with the previous reports [29,47]. Similar to these reports, we speculate that the provided surface structure endows anisotropic wetting properties and potentially brings about self-cleaning to the devices. Furthermore, while the usage of leek leaf was shown to improve the efficiency of the encapsulated devices, the presented method is not limited to this certain bio-template. Therefore, despite its simplicity, the versatility of the developed technique

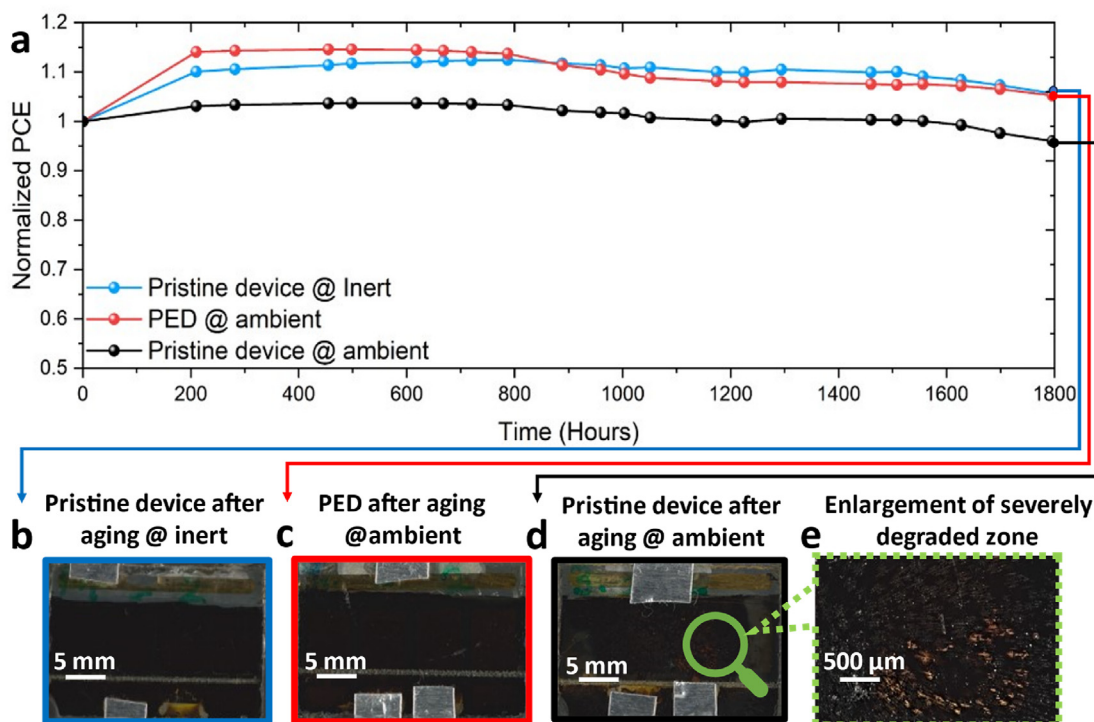
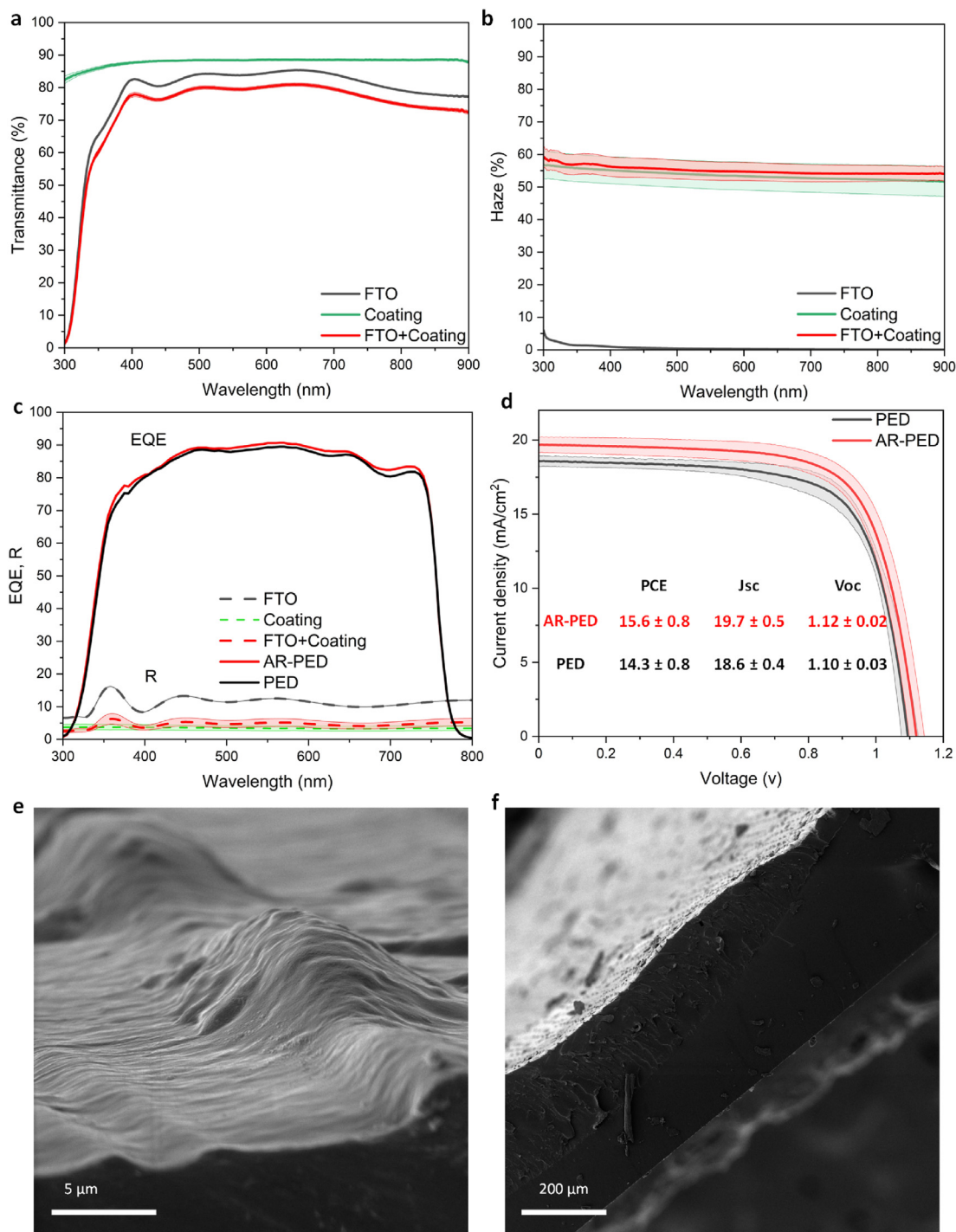


Fig. 5. The long-term stability of PEDs, pristine devices, and the devices kept in an inert environment, b) the aged PSC that was in the inert atmosphere during the test, c) the aged PED, d) the aged pristine device, e) the magnified image of the new patterns. PED: polydimethylsiloxane-encapsulated devices; PSC: perovskite solar cell.



**Fig. 6.** Comparison of the optical properties of FTO glass, antireflective coating, and coated FTO glass, illustrating the a) transmittance, b) haze, c) reflectance, and EQE (averaged over three measurements and the bands show standard deviations, the errors in the EQE spectra are so small that they are not visible in the graph.), d) the average J-V curves of PEDs and AR-PEDs (averaged over five devices and the bands show standard deviations), and SEM images showing the e) lateral view and, f) cross-section of the patterned PDMS. EQE: external quantum efficiency; FTO: fluorine-doped tin oxide; AR-PED: antireflective polydimethylsiloxane-encapsulated devices.

enables the integration of virtually any surface pattern with encapsulation.

#### 4. Conclusion

In conclusion, this study introduced a one-step encapsulation approach using polydimethylsiloxane for perovskite solar cells, addressing both optical losses and extrinsic stability issues

simultaneously. By systematically investigating the impact of encapsulation on device performance under elevated humidity and outdoor conditions, the encapsulated devices demonstrated significant protection against moisture and oxygen ingress. These devices exhibited superior operational stability, retaining almost 80 % of their initial performance even after prolonged exposure to light, outperforming their pristine counterparts. Furthermore, our approach integrates an antireflective coating onto the encapsulated

PSCs using a soft lithography technique, enhancing their light-harvesting capability and improving performance. This dual-function method resulted in an  $8\% \pm 0.8$  enhancement in power conversion efficiency, attributed to reduced reflection losses and increased light absorption through higher haze. The simplicity and effectiveness of the proposed encapsulation and patterning method, which does not require high temperature curing or intricate equipment, offer promise for scalable and cost-effective production. By seamlessly combining encapsulation with patterning in a single-step, this approach addresses both instability and optical loss, underscoring its potential for the photovoltaic industry and facilitating the realization of stable and efficient perovskite solar cells for future solar energy applications.

### CRedit authorship contribution statement

**Seyede Maryam Mousavi:** Writing – review & editing, Writing – original draft, Visualization, Methodology, Investigation, Formal analysis, Data curation, Conceptualization, Validation, Funding acquisition. **Hamidreza Daghigh Shirazi:** Writing – review & editing, Writing – original draft, Funding acquisition, Visualization, Validation, Methodology, Formal analysis, Conceptualization. **Rikhard Ranta:** Writing – original draft, Investigation. **Muhammad Imran Asghar:** Writing – review & editing, Methodology. **Severi Kasurinen:** Methodology. **Janne Halme:** Writing – review & editing, Resources, Project administration, Methodology, Investigation. **Jaana Vapaavuori:** Writing – review & editing, Validation, Supervision, Project administration, Methodology, Investigation, Funding acquisition, Formal analysis, Conceptualization.

### Declaration of competing interest

The authors declare that they have no known competing financial interests or personal relationships that could have appeared to influence the work reported in this paper.

### Acknowledgment

SMM and JV would acknowledge the financial support from Neste and Fortum Foundation (Grant No. 20230089) and the PREIN flagship project (Decision number: 346529) for the generous funding. HDS and JV acknowledge the Academy of Finland's Flagship Programme under Projects No. 318890 and 318891 (Competence Center for Materials Bioeconomy, FinnCERES), as well as European Research Council (H2020) project "ModelCom" (Decision number 949648).

### Data availability

Data will be made available on request.

### Appendix A. Supplementary data

Supplementary data to this article can be found online at <https://doi.org/10.1016/j.mtener.2024.101707>.

### References

- [1] F.J. Nijssse, J.-F. Mercure, N. Ameli, F. Larosa, S. Kothari, J. Rickman, P. Vercoolen, H. Pollitt, The momentum of the solar energy transition, *Nat. Commun.* 14 (2023) 6542.
- [2] NREL. 2023 [cited 2023 October 24]; Available from: <https://www.nrel.gov/pv/cell-efficiency.html>.
- [3] L. Shen, Y. Yang, T. Zhu, L. Liu, J. Zheng, X. Gong, Efficient and stable perovskite solar cells by B-site compositional engineered all-inorganic perovskites and interface passivation, *ACS Appl. Mater. Interfaces* 14 (2022) 19469–19479.
- [4] S.M. Mousavi, M. Alidaei, F.A. Roghabadi, V. Ahmadi, S.M. Sadrameli, J. Vapaavuori, Stability improvement of MAPbI<sub>3</sub>-based perovskite solar cells using a photoactive solid-solid phase change material, *J. Alloys Compd.* 897 (2022) 163142.
- [5] M.K. Mohammed, A.K. Al-Mousoi, S. Singh, U. Younis, A. Kumar, D. Dastan, G. Ravi, Ionic liquid passivator for mesoporous titanium dioxide electron transport layer to enhance the efficiency and stability of hole conductor-free perovskite solar cells, *Energy Fuels* 36 (2022) 12192–12200.
- [6] J. Zhou, M. Lyu, J. Zhu, G. Li, Y. Li, S. Jin, J. Song, H. Niu, J. Xu, R. Zhou, SnO<sub>2</sub> quantum dot-modified mesoporous TiO<sub>2</sub> electron transport layer for efficient and stable Perovskite solar cells, *ACS Appl. Energy Mater.* 5 (2022) 3052–3063.
- [7] X. Chen, B. Guo, Z. Zhang, B. Zhang, X. Zu, N.A.N. Ouedraogo, J. Oh, Y. Cho, G.O. Odunmbaku, K. Chen, Binary hole transport layer enables stable perovskite solar cells with PCE exceeding 24, *DeCarbon* 1 (2023) 100004.
- [8] Y. Kim, G. Kim, E.Y. Park, C.S. Moon, S.J. Lee, J.J. Yoo, S. Nam, J. Im, S.S. Shin, N.J. Jeon, Alkylammonium bis (trifluoromethylsulfonyl) imide as a dopant in the hole-transporting layer for efficient and stable perovskite solar cells, *Energy Environ. Sci.* 16 (2023) 2226–2238.
- [9] X. Lin, H. Su, S. He, Y. Song, Y. Wang, Z. Qin, Y. Wu, X. Yang, Q. Han, J. Fang, In situ growth of graphene on both sides of a Cu–Ni alloy electrode for perovskite solar cells with improved stability, *Nat. Energy* 7 (2022) 520–527.
- [10] C. Chen, H. Bala, S. Yao, B. Zhang, N. Sha, X. An, W. Zhang, D. Chen, Enhanced efficiency and stability of perovskite solar cells based on carbon-counter-electrode via anti-solvent treatment, *J. Alloys Compd.* 920 (2022) 165874.
- [11] F.A. Roghabadi, M. Alidaei, S.M. Mousavi, T. Ashjari, A.S. Tehrani, V. Ahmadi, S.M. Sadrameli, Stability progress of perovskite solar cells dependent on the crystalline structure: from 3D ABX<sub>3</sub> to 2D Ruddlesden–Popper perovskite absorbers, *J. Mater. Chem. A* 7 (2019) 5898–5933.
- [12] M. Mohammadi, S. Gholipour, M. Malekshahi Byranvand, Y. Abdi, N. Taghavinia, M. Saliba, Encapsulation strategies for highly stable perovskite solar cells under severe stress testing: damp heat, freezing, and outdoor illumination conditions, *ACS Appl. Mater. Interfaces* 13 (2021) 45455–45464.
- [13] T. Leijtens, G.E. Eperon, N.K. Noel, S.N. Habisreutinger, A. Petrozza, H.J. Snaith, Stability of metal halide perovskite solar cells, *Adv. Energy Mater.* 5 (2015) 1500963.
- [14] Y.-B. Lu, W.-Y. Cong, C. Guan, H. Sun, Y. Xin, K. Wang, S. Song, Light enhanced moisture degradation of perovskite solar cell material CH<sub>3</sub>NH<sub>3</sub>PbI<sub>3</sub>, *J. Mater. Chem. A* 7 (2019) 27469–27474.
- [15] L. Duan, A. Uddin, Defects and stability of perovskite solar cells: a critical analysis, *Mater. Chem. Front.* 6 (2022) 400–417.
- [16] L. Liao, J. Bo, Z. Guo, C. Wang, B. Fan, W. Ge, R. Peng, Fullerene derivatives barrier layer for efficient and stable perovskite solar cells through interfacial modification and removal of superoxide radicals, *Carbon* 226 (2024) 119173.
- [17] S.-K. Jung, N.-G. Park, J.-W. Lee, Light management in perovskite solar cells, *Mater. Today Energy* (2023) 101401.
- [18] D.I. Kim, J.W. Lee, R.H. Jeong, J.W. Yang, S. Park, J.-H. Boo, Optical and water-repellent characteristics of an anti-reflection protection layer for perovskite solar cells fabricated in ambient air, *Energy* 210 (2020) 118582.
- [19] M.M. Tavakoli, K.-H. Tsui, Q. Zhang, J. He, Y. Yao, D. Li, Z. Fan, Highly efficient flexible perovskite solar cells with antireflection and self-cleaning nanostructures, *ACS Nano* 9 (2015) 10287–10295.
- [20] H. Lee, A. Yi, J. Choi, D.-H. Ko, H.J. Kim, Texturing of polydimethylsiloxane surface for anti-reflective films with super-hydrophobicity in solar cell application, *Appl. Surf. Sci.* 584 (2022) 152625.
- [21] D. Du, Z. Xu, L. Wang, Y. Guo, S. Liu, T. Yu, C. Wang, F. Wang, H. Wang, The broadband and omnidirectional antireflective performance of perovskite solar cells with curved nanostructures, *Sol. Energy* 224 (2021) 10–17.
- [22] K. Li, Y. Zhang, H. Zhen, H. Wang, S. Liu, F. Yan, Z. Zheng, Versatile biomimetic haze films for efficiency enhancement of photovoltaic devices, *J. Mater. Chem. A* 5 (2017) 969–974.
- [23] S.M.M. Hamidreza Daghigh Shirazi, Seyede Maryam Mousavi, Magnus Markkanen, Janne Halme, Ville Jokinen, Jaana Vapaavuori, From Kitchen Garden to Multifunctionality: Leek-Inspired Surface Structures Introduce Optical and Self-Cleaning Properties to Cellulose-Based Films, in *Research Square*, A. University, Editor, 2023.
- [24] E.Y. Choi, J.-H. Kim, B.-J. Kim, J.H. Jang, J. Kim, N. Park, Development of moisture-proof polydimethylsiloxane/aluminum oxide film and stability improvement of perovskite solar cells using the film, *RSC Adv.* 9 (2019) 11737–11744.
- [25] M.H. Park, J.Y. Kim, T.H. Han, T.S. Kim, H. Kim, T.W. Lee, Flexible lamination encapsulation, *Adv. Mater.* 27 (2015) 4308–4314.
- [26] Y. Shi, F. Zhang, Advances in encapsulations for perovskite solar cells: from materials to applications, *Sol. RRL* 7 (2023) 2201123.
- [27] Q. Emery, M. Remec, G. Paramasivam, S. Janke, J. Dagar, C. Ulbrich, R. Schlattmann, B. Stannowski, E. Unger, M. Khenkin, Encapsulation and outdoor testing of perovskite solar cells: comparing industrially relevant process with a simplified lab procedure, *ACS Appl. Mater. Interfaces* 14 (2022) 5159–5167.
- [28] M.-c. Kim, S. Jang, J. Choi, S.M. Kang, M. Choi, Moth-eye structured polydimethylsiloxane films for high-efficiency perovskite solar cells, *Nano-Micro Lett.* 11 (2019) 1–10.
- [29] H. Daghigh Shirazi, S.M. Mirmohammadi, S.M. Mousavi, M. Markkanen, J. Halme, V. Jokinen, J. Vapaavuori, Bio-inspired surface structures promote

- optical transmittance and hydrophobicity in cellulose-based films for self-cleaning perovskite solar cells, *Communications Materials* 5 (2024) 88.
- [30] M. Saliba, J.-P. Correa-Baena, C.M. Wolff, M. Stollerfoht, N. Phung, S. Albrecht, D. Neher, A. Abate, How to make over 20% efficient perovskite solar cells in regular (n-i-p) and inverted (p-i-n) architectures, *Chem. Mater.* 30 (2018) 4193–4201.
- [31] Z. Wang, Z. Zhang, L. Xie, S. Wang, C. Yang, C. Fang, F. Hao, Recent advances and perspectives of photostability for halide perovskite solar cells, *Adv. Opt. Mater.* 10 (2022) 2101822.
- [32] M.V. Khenkin, E.A. Katz, A. Abate, G. Bardizza, J.J. Berry, C. Brabec, F. Brunetti, V. Bulović, Q. Burlingame, A. Di Carlo, Consensus statement for stability assessment and reporting for perovskite photovoltaics based on ISOS procedures, *Nat. Energy* 5 (2020) 35–49.
- [33] E.V. Péan, C.S. De Castro, S. Dimitrov, F. De Rossi, S. Meroni, J. Baker, T. Watson, M.L. Davies, Investigating the superoxide formation and stability in mesoporous carbon perovskite solar cells with an aminovaleric acid additive, *Adv. Funct. Mater.* 30 (2020) 1909839.
- [34] N. Aristidou, C. Eames, I. Sanchez-Molina, X. Bu, J. Kosco, M.S. Islam, S.A. Haque, Fast oxygen diffusion and iodide defects mediate oxygen-induced degradation of perovskite solar cells, *Nat. Commun.* 8 (2017) 15218.
- [35] J. Zhuang, J. Wang, F. Yan, Review on chemical stability of lead halide perovskite solar cells, *Nano-Micro Lett.* 15 (2023) 84.
- [36] C.-T. Lin, F. De Rossi, J. Kim, J. Baker, J. Ngiam, B. Xu, S. Pont, N. Aristidou, S.A. Haque, T. Watson, Evidence for surface defect passivation as the origin of the remarkable photostability of unencapsulated perovskite solar cells employing aminovaleric acid as a processing additive, *J. Mater. Chem. A* 7 (2019) 3006–3011.
- [37] R.T. Ginting, E.-S. Jung, M.-K. Jeon, W.-Y. Jin, M. Song, J.-W. Kang, Low-temperature operation of perovskite solar cells: with efficiency improvement and hysteresis-less, *Nano Energy* 27 (2016) 569–576.
- [38] F. Gao, W. Tress, J. Wang, O. Inganäs, Temperature dependence of charge carrier generation in organic photovoltaics, *Phys. Rev. Lett.* 114 (2015) 128701.
- [39] Y. Nakamura, N. Shibayama, K. Fujiwara, T. Koganezawa, T. Miyasaka, Degradation mechanism of halide perovskite crystals under concurrent light and humidity exposure, *ACS Mater. Lett.* 4 (2022) 2409–2414.
- [40] R.A. Scheidt, E. Kerns, P.V. Kamat, Interfacial charge transfer between excited CsPbBr<sub>3</sub> nanocrystals and TiO<sub>2</sub>: charge injection versus photodegradation, *J. Phys. Chem. Lett.* 9 (2018) 5962–5969.
- [41] M.V. Khenkin, A. Km, I. Visoly-Fisher, S. Kolusheva, Y. Galagan, F. Di Giacomo, O. Vukovic, B.R. Patil, G. Sherafatipour, V. Turkovic, Dynamics of photoinduced degradation of perovskite photovoltaics: from reversible to irreversible processes, *ACS Appl. Energy Mater.* 1 (2018) 799–806.
- [42] X. Li, M. Tschumi, H. Han, S.S. Babkair, R.A. Alzubaydi, A.A. Ansari, S.S. Habib, M.K. Nazeeruddin, S.M. Zakeeruddin, M. Grätzel, Outdoor performance and stability under elevated temperatures and long-term light soaking of triple-layer mesoporous perovskite photovoltaics, *Energy Technol.* 3 (2015) 551–555.
- [43] V.V. Ozerova, N.A. Emelianov, L.G. Gutsev, D.V. Korchagin, G.V. Shilov, N.N. Dremova, B.R. Ramachandran, A.Y. Sukhorukov, S.M. Aldoshin, L.A. Frolova, Enhanced photostability of multication lead halide perovskites through the use of azaadamantane-based modifiers, *Mater. Today Chem.* 30 (2023) 101590.
- [44] T. Sekimoto, R. Uchida, M. Hiraoka, T. Matsui, R. Kikuchi, T. Nakamura, T. Yamamoto, K. Kawano, T. Negami, Y. Kaneko, Investigation of the acceleration and suppression of the light-induced degradation of a lead halide perovskite solar cell using hard X-ray photoelectron spectroscopy, *ACS Appl. Energy Mater.* 5 (2022) 4125–4137.
- [45] K. Sun, R. Guo, Y. Liang, J.E. Heger, S. Liu, S. Yin, M.A. Reus, L.V. Spanier, F. Deschler, S. Bernstorff, Morphological insights into the degradation of perovskite solar cells under light and humidity, *ACS Appl. Mater. Interfaces* 15 (2023) 30342–30349.
- [46] F. Schneider, J. Draheim, R. Kamberger, U. Wallrabe, Process and material properties of polydimethylsiloxane (PDMS) for Optical MEMS, *Sensor Actuator Phys.* 151 (2009) 95–99.
- [47] S.M. Mirmohammadi, H.D. Shirazi, M. Heikkilä, S. Franssila, J. Vapaavuori, V. Jokinen, Anisotropic superhydrophobic properties replicated from leek leaves, *Small* (2024) 2403863.
- [48] J.W. Leem, Y.M. Song, J.S. Yu, Biomimetic artificial Si compound eye surface structures with broadband and wide-angle antireflection properties for Si-based optoelectronic applications, *Nanoscale* 5 (2013) 10455–10460.
- [49] G. Li, J. Li, C. Zhang, Y. Hu, X. Li, J. Chu, W. Huang, D. Wu, Large-area one-step assembly of three-dimensional porous metal micro/nanocages by ethanol-assisted femtosecond laser irradiation for enhanced antireflection and hydrophobicity, *ACS Appl. Mater. Interfaces* 7 (2015) 383–390.
- [50] H.K. Raut, S.S. Dinachali, Y.C. Loke, R. Ganesan, K.K. Anshah-Antwi, A. Gora, E.H. Khoo, V.A. Ganesh, M.S. Saifullah, S. Ramakrishna, Multiscale ommatidial arrays with broadband and omnidirectional antireflection and antifogging properties by sacrificial layer mediated nanoimprinting, *ACS Nano* 9 (2015) 1305–1314.
- [51] Y.M. Song, G.C. Park, S.J. Jang, J.H. Ha, J.S. Yu, Y.T. Lee, Multifunctional light escaping architecture inspired by compound eye surface structures: from understanding to experimental demonstration, *Opt Express* 19 (2011) A157–A165.
- [52] J.-Q. Xi, M.F. Schubert, J.K. Kim, E.F. Schubert, M. Chen, S.-Y. Lin, W. Liu, J.A. Smart, Optical thin-film materials with low refractive index for broadband elimination of Fresnel reflection, *Nat. Photonics* 1 (2007) 176–179.